

Black hole accretion of scalar clouds with spontaneous symmetry breaking

Sebastian Garcia-Saenz,¹ Guangzhou Guo,¹ Peng Wang,² and Xinmiao Wang¹

¹*Department of Physics, Southern University of Science and Technology, Shenzhen 518055, China*

²*Center for Theoretical Physics, College of Physics, Sichuan University, Chengdu 610064, China*

Spontaneous scalarization of black holes typically occurs through the condensation of a scalar field, with the field evolving from a $U(1)$ -symmetric phase into a symmetry-breaking one with lower energy. We show that there exist symmetry-breaking phases which are themselves unstable to the formation of an additional scalar condensate, or ‘cloud’, which is partly accreted into the black hole. By studying the fully nonlinear dynamical evolution of the process, we find that symmetry breaking causes the accretion channels of scalar clouds to be non-degenerate, favoring a dominant channel for evolution. Additionally, the final states form a characteristic energy band due to varying amounts of radiation emitted by clouds in different channels.

I. INTRODUCTION

The past decade has witnessed spectacular progress in the field of black hole physics, driven primarily by the detection of gravitational waves from binary black hole mergers, which opened up new avenues for exploring the properties of black holes [1]. Prime among these is the testing of the validity of the black hole uniqueness theorems of general relativity (see [2] for a review), particularly through the measurement of quasinormal modes during the ringdown phase [3, 4]. The Event Horizon Telescope has similarly revolutionized our understanding of black holes by capturing the images of M87* and Sgr A* [5, 6], revealing a striking feature: a luminous ring encircling a dark shadow. These distinctive signatures have been attributed to the intense light deflection occurring near unstable bound photon orbits, providing insights into black hole physics in the strong field regime, e.g. the structure of luminous accretion disks [7–11].

While these phenomena align with the predictions of general relativity [12–14], future observations of increased precision offer the exciting prospect of measuring deviations from Einstein’s gravity interacting with standard matter [15]. For instance, the no-hair theorem [16, 17] may be circumvented in the presence of a scalar field that couples non-minimally either to gravity or to other matter fields [18–20]. In this well-studied setup, black holes are subject to the growth of ‘hair’ in the form of a scalar cloud, i.e. a nonstatic, but potentially long-lived, condensate of the field in the vicinity of the event horizon.¹ Although originally studied in the context of neutron stars [25], this so-called spontaneous scalarization phenomenon has been shown to also arise in black

hole spacetimes within scalar-tensor theories of gravity, the best-known model being scalar-tensor-Gauss-Bonnet theory and its extensions [26–30].

On the other hand, it has been appreciated that scalarization may occur in a simpler class of models, which feature no higher curvature terms and only minimal gravitational couplings, but they require the presence of an additional matter field with which the scalar interacts non-minimally. A very natural choice in this class is the Einstein-Maxwell-scalar (EMS) theory where the scalar field Φ couples to the standard Einstein-Maxwell Lagrangian through the term $f(|\Phi|)F^{\mu\nu}F_{\mu\nu}$, with $F_{\mu\nu}$ the electromagnetic field strength and f some function [31] (see also [32] for earlier work in the context of nonlinear electrodynamics). The spontaneous scalarization effect in the EMS model has been further studied in [33–36], while various properties of these scalarized black holes have been investigated in [37–40], along with their spinning counterparts [41, 42].

Scalarization in the EMS model occurs dynamically through a tachyonic (i.e. negative effective potential) instability of an initial scalar field perturbation on the background of a hairless black hole, driving the system into a new configuration with lower energy accompanied by a non-trivial scalar field distribution. In this paper we ignore spin, so the initial state is a Reissner-Nordström (RN) black hole; notice that electric charge is needed to trigger the destabilization effect [31]. The appearance of a nontrivial scalar profile, or condensate, may be naturally understood as a process of spontaneous symmetry breaking. In the original setup, the scalar field is real, so the symmetry that is broken by the scalarization effect is \mathbb{Z}_2 , or $\Phi \mapsto -\Phi$. Here we focus instead on the case of a complex scalar as it provides a more interesting symmetry breaking pattern, namely that of a (global) $U(1)$ symmetry. The study of spontaneous scalarization in this scenario has been pioneered in [43, 44].

In this paper, we employ numerical relativity to investigate the fully nonlinear dynamics of the EMS model, specifically the spontaneous scalarization of a charged black hole and the subsequent evolution of the scalar cloud. After its initial formation following the tachyonic destabilization, we observe that the cloud continues to

¹ The term ‘scalar cloud’, or more generally ‘boson cloud’, appears to be mostly used in the context of rotating black holes, where a scalar condensate forms as a result of superradiance; see e.g. [21–23] for recent work and [24] for the electromagnetic analog. We apply this terminology here too, which is justified because the clouds formed via scalarization are also nonstatic and evolve through accretion and radiation. We emphasize however that, unlike in most previous studies, our numerical treatment of the cloud is fully nonlinear and does not neglect backreaction.

evolve, on a timescale of order the distance between the cloud and the event horizon, in a process of energy loss both to accretion into the black hole and ejection to spatial infinity. We find essential differences between the scenario where scalarization occurs starting in a symmetric phase, i.e. without further instabilities upon formation of a scalar condensate, versus the case where a scalar cloud forms from a symmetry-broken phase. Unlike with scalarization from the symmetric phase, the breaking of $U(1)$ symmetry allows for multiple accretion channels for the cloud, each leading to different amounts of energy loss and distinct final states. Notably, a dominant accretion channel emerges due to symmetry breaking.

II. SCALARIZATION

We consider the EMS model of [31], extended here to a complex scalar field $\Phi = \phi_1 + i\phi_2$, which is non-minimally coupled to the electromagnetic field A_μ . The complete action is (we use geometrized units with $G = c = 1$)

$$S = \frac{1}{16\pi} \int d^4x \sqrt{-g} [R - 2\partial_\mu \Phi^* \partial^\mu \Phi - f(|\Phi|) F^{\mu\nu} F_{\mu\nu}], \quad (1)$$

where $F_{\mu\nu} = \partial_\mu A_\nu - \partial_\nu A_\mu$. In this paper, we adopt $f(|\Phi|) = e^{\alpha|\Phi|^2}$ for the non-minimal coupling function, with α a real constant, a choice which admits an electrovacuum solution given by a RN black hole and $\Phi = 0$.² Note that we do not include a minimal coupling of the scalar field to electromagnetism, i.e. Φ is uncharged under the electromagnetic $U(1)$, unrelated to the global $U(1)$ symmetry $\Phi \mapsto e^{i\varphi}\Phi$. The electrovacuum solution preserves the $U(1)$ symmetry, so we refer to it as the symmetric phase.

A small scalar perturbation $\delta\Phi$ on the RN black hole background obeys the equation $(\square - \mu_{\text{eff}}^2) \delta\Phi = 0$, where $\mu_{\text{eff}}^2 \equiv -\alpha Q^2/r^4$ (r is the radius in standard spherical coordinates) and Q is the charge of the hole. If $\alpha > 0$, the negative value of μ_{eff}^2 introduces a tachyonic effect, potentially destabilizing the background and triggering scalarization.

More in detail, and considering now a general static and spherically symmetric ansatz for the metric, $ds^2 = -e^{-2\delta(r)} N(r) dt^2 + dr^2/N(r) + r^2 d\Omega^2$, one finds the equation $\frac{d^2\Psi}{dx^2} + (\omega^2 - V_{\text{eff}}(x)) \Psi = 0$ obeyed by the spherical, or monopole, perturbation $\Psi \equiv r\delta\Phi$, where ω is the frequency, x is defined by $dx/dr \equiv e^{\delta(r)}/N(r)$ and

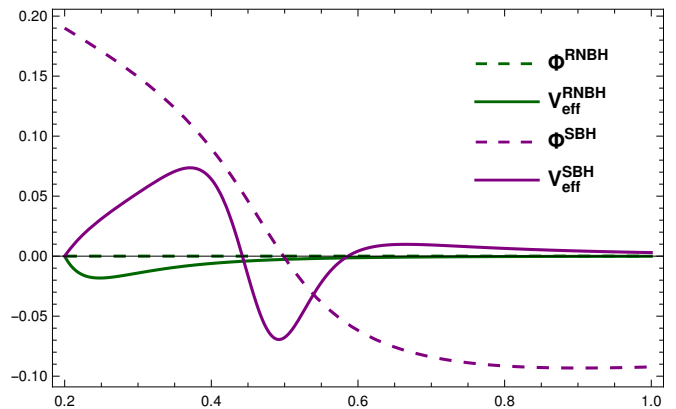


FIG. 1. Scalar field profiles (dashed lines) and effective potentials (solid) for $Q/M = 0.55$ RN (green) and $Q/M = 1.29$ scalarized (purple) black holes, respectively. The event horizons are set at $r_h = 0.2$. Both the RN and scalarized black holes (SBH) possess negative potential wells. In the latter case, the well is separated from the horizon by a potential barrier, and its location coincides with the node of the scalar field.

V_{eff} is the effective potential.³ In Fig. 1, the effective potential for the $U(1)$ -symmetric phase is seen to display a negative well near the event horizon, and a numerical calculation shows that a tachyon mode with $\omega = 0.2454iM$ is present. In agreement with expectations, this mode is responsible for triggering spontaneous scalarization [31, 45]. Intriguingly, we find that there exist $U(1)$ -broken phases (scalarized black holes with $\Phi \neq 0$), which also exhibit a negative potential well, a feature that is linked to the presence of a node in the scalar profile. This suggests that these symmetry-breaking phases are unstable to the formation of a scalar cloud localized around the potential well. Our aim in this paper is to advance the investigation of the nonlinear dynamics of scalar clouds to encompass both $U(1)$ -symmetric and $U(1)$ -broken phases.

III. DYNAMICAL FORMATION OF SCALAR CLOUDS

To simulate the fully nonlinear evolution in the EMS model, we use the Baumgarte-Shapiro-Shibata-Nakamura (BSSN) formulation implemented in *BlackHoles@Home* [46]; see [47–52] for references and Appendix A for some technical details and numerical convergence tests. To ensure consistent numerical results,

² More generally, the function $f(|\Phi|)$ must satisfy $f'' > 0$ and $|\Phi|f' > 0$ (here primes denotes derivatives of f with respect to its argument) for some range of the radial coordinate [31]. In addition, $f'(0) = 0$ in order for the model to admit hairless solutions.

³ Explicitly,

$$V_{\text{eff}} = \frac{N}{r^2 e^{2\delta}} \left[1 - N - 2r^2 |\Phi'|^2 - \frac{Q^2 (1 + \alpha - 2|\alpha\Phi - r\Phi'|^2)}{r^2 e^{\alpha|\Phi|^2}} \right].$$

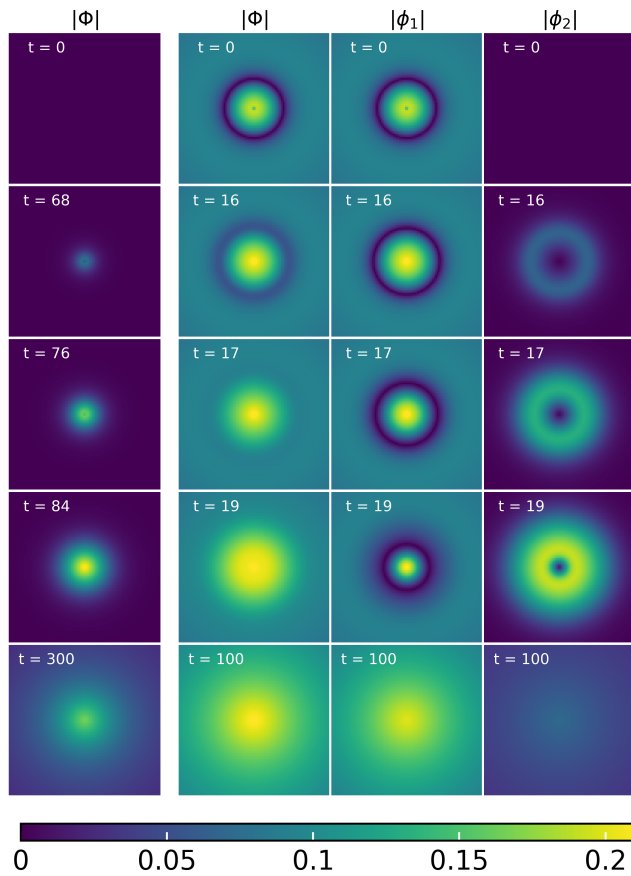


FIG. 2. Dynamical formation of a scalar cloud for the initial perturbation with $\theta_0 = \pi/2$ in the $U(1)$ -symmetric ($M = 2.5$, leftmost column) and $U(1)$ -broken ($\Phi_h = 0.19$ and $M = 0.7744$, right columns) phases. A scalar cloud develops within the negative potential well due to scalarization and is subsequently accreted onto the black hole, terminating in the formation of a stable cloud structure around it.

we also perform nonlinear simulations with the *Einstein Toolkit* [53]. Given our focus on spherically symmetric evolution, we have the electromagnetic field $A_\mu = A(t, r)\delta_\mu^t$ (choosing the gauge $A_r = 0$), and from the equations of motion one infers $\partial_\mu(\sqrt{-g}e^{\alpha\Phi^*}\partial^r A^t) = 0$, indicating that the black hole charge Q , defined by the integration constant, is conserved during temporal evolution. For our numerical study, we set units such that $Q = 1$ and $\alpha = 160$.⁴ For the initial data, we introduce a scalar perturbation $\delta\Phi = pe^{-\frac{(r-r_0)^2}{\Delta^2}}e^{i\theta_0}$ around both the $U(1)$ -symmetric and $U(1)$ -broken phases. Here, θ_0 is the phase factor of the perturbation, the amplitude is chosen as $p = 10^{-6}$, the location r_0 is set around the negative potential well, and the width is chosen as $\Delta = 1$. For latter

⁴ Although the tachyonic instability does not require very large values of α , such a choice makes the instability rate faster and thus easier to simulate numerically.

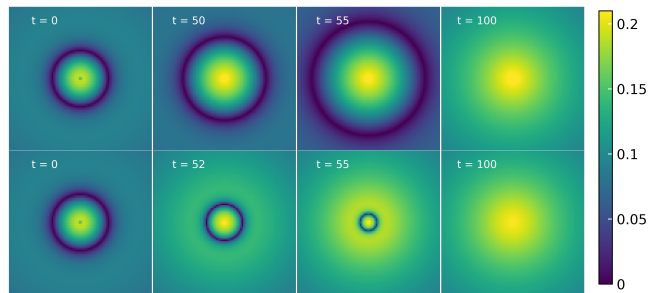


FIG. 3. Dynamical evolution of the field norm $|\Phi|$ for initial perturbations with $\theta_0 = 0$ (upper row) and $\theta_0 = \pi$ (lower) in the symmetry-broken phase ($\Phi_h = 0.19$ and $M = 0.7744$). The scalar cloud formed from the positive perturbation ($\theta_0 = 0$) can induce nonlinear effects at late times, causing the scalar field node to propagate towards spatial infinity. Conversely, the negative perturbation ($\theta_0 = \pi$) leads to the node of the field moving into the event horizon at late times, resulting in a stable, nodeless scalar distribution outside the black hole.

use, we define Φ_h to be the (time-dependent) value of the scalar field Φ at the event horizon. At the background level, i.e. prior to the introduction of the above perturbation $\delta\Phi$, the $U(1)$ -breaking system is chosen, without loss of generality, to have a real and positive value of Φ .

In Fig. 2, an initial wavepacket with phase $\theta_0 = \pi/2$, perturbing only the field component ϕ_2 , is placed within the negative potential well. In the symmetric phase, the field amplitude $|\Phi|$ grows near the event horizon, forming a scalar cloud within the potential well. Ultimately, a long-lived cloud accretes onto the black hole, with the evolution terminating in a scalarized black hole, consistent with the results of [31, 45]. In the $U(1)$ -broken phase, the negative potential well is separated from the horizon of the scalarized black hole (with $\Phi_h = 0.19$ in our simulation). The perturbation grows via tachyonic instabilities, forming a ring structure for ϕ_2 around the well (see the rightmost column). After approximately $t \approx 20$ in our numerics, the cloud becomes massive enough and is drawn into the black hole by the gravitational pull. As a result, the cloud component ϕ_2 is gradually accreted onto the hole, forming a lighter cloud that remains near the horizon in equilibrium, i.e. a hairy black hole. During this process, the node of the scalar field $|\Phi|$ gradually fades as the ϕ_2 cloud forms and eventually disappears.

While in the symmetric phase the dynamics remain $U(1)$ -equivalent, in the symmetry-broken phase the accretion process can vary significantly based on the initial perturbation phase. In Fig. 3, we exhibit the evolution of the scalar field for perturbations with $\theta_0 = 0$ and $\theta_0 = \pi$, neither of which induces a scalar cloud in the ϕ_2 direction. For the $\theta_0 = 0$ perturbation, a cloud of positive ϕ_1 accumulates within the potential well. As the cloud grows, non-linear effects cause the node of Φ to propagate towards spatial infinity. A similar scenario occurs for the $\theta_0 = \pi$ perturbation, now with a cloud of nega-

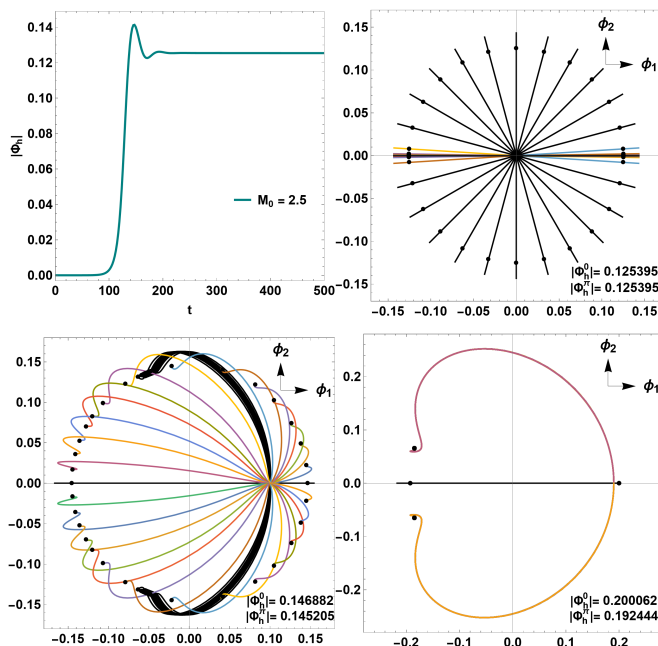


FIG. 4. Channels of scalar cloud accretion, represented by the value of the scalar field at the event horizon, Φ_h . *Upper row*: In the $U(1)$ -symmetric phase ($\Phi = 0$ and $M = 2.5$), the accretion dynamics and final states remain $U(1)$ -symmetric with respect to the initial perturbation phase θ_0 . *Lower*: In the $U(1)$ -broken phases, using here $\Phi_h = 0.1$, $M = 1.8744$ (left panel) and $\Phi_h = 0.19$, $M = 0.7744$ (right panel), the accretion paths no longer respect the $U(1)$ symmetry. Cloud accretion tends to follow a dominant path, a phenomenon that becomes more pronounced for larger Φ_h values of the initial field: in the right panel, the black and colored lines almost completely overlap (the visible purple and orange lines cover all other colored as well as black lines). As a result, the final states are not $U(1)$ -symmetric, as indicated by the varying values of $|\Phi_h|$ shown in the lower right corners.

tive ϕ_1 , driving the node of Φ inward towards the black hole. In both cases, the formation and accretion of scalar clouds effectively peel off the negative potential well and “radiate” the node of the field.

To further explore the relationship between the dynamical accretion of scalar clouds and the initial perturbation phase θ_0 , we systematically examine the evolution of the scalar field at the event horizon, $\Phi_h(t)$, for a range of θ_0 values. In Figs. 4 and 5, 24 uniformly spaced values (black lines) within the interval $(0, 2\pi)$, as well as a set of specific values (colored lines) within the narrower intervals $(-\pi/12, \pi/12)$ and $(11\pi/12, 13\pi/12)$. In the symmetric phase, we observe that the accretion process of the cloud manifests the $U(1)$ symmetry, as depicted in the upper row of Fig. 4, which shows in particular the conservation of the phase θ during time evolution. On the other hand, in the $U(1)$ -broken phase, the symmetry breaking causes the phase factor θ to become a non-trivial dynamical variable during the accretion, as illustrated in the lower panels of Fig. 4. We observe a manifest loss

of $U(1)$ invariance in the process, although it remains symmetric with respect to the ϕ_1 -axis due to a residual \mathbb{Z}_2 symmetry.⁵ Interestingly, the symmetry breaking introduces a preferred path for scalar cloud accretion, acting as an attractor that draws in the majority of accretion channels. Fig. 2 illustrates one such typical path ($\theta_0 = \pi/2$). Furthermore, the final equilibrium state will not be $U(1)$ -symmetric for scalar clouds in the symmetry-broken phase. As shown in the lower right corner of the lower panels, we find that $|\Phi_h^{\theta_0}|$, which represents the value of $|\Phi_h|$ at the end state for a given initial perturbation phase θ_0 , is maximal for $\theta_0 = 0$ and minimal for $\theta_0 = \pi$ (see also Fig. 5).

The existence of a dominant path in field space may be understood from the fact that one expects most of the energy of the field to go into the gapless degrees of freedom, in this case the angular component of Φ , with a comparatively smaller fraction in the radial field.⁶ This picture is consistent with the observed trajectory, which appears to be roughly circular, at least qualitatively. This intuition is corroborated by an explicit comparison of the energy densities stored in the radial and angular components of the field; see Appendix B for details.

IV. ENERGY LOSS

A noteworthy phenomenon during scalar cloud accretion is that the cloud reaches equilibrium after a portion of its energy is radiated to spatial infinity (see Figs. 2 and 3), potentially causing the final state to have less energy than the initial state. In Fig. 5, we calculate the Arnowitt-Deser-Misner mass [54] of the initial and final states to quantify the energy loss during accretion in both the $U(1)$ -symmetric and $U(1)$ -breaking phases. In both cases, a discernible energy gap exists between the initial and final states, confirming that the formation of a stable scalar cloud involves the radiation of energy to spatial infinity.

In the symmetric phase, the end states maintain the $U(1)$ -symmetry and are degenerate with respect to the final energy ($M_1 = 2.4816$ in our numerics). The energy loss, calculated as $M_1 - M_0$ (displayed in the table of Fig. 5), indicates a transition from the $U(1)$ -symmetric phase to a lower-energy final state. On the other hand, in the $U(1)$ -broken phase, symmetry breaking lifts this degeneracy and leads to an energy band for the final states, bounded by the cases with initial phases $\theta_0 = 0$ and $\theta_0 = \pi$. Notably, the $\theta_0 = 0$ perturbation induces the formation of a positive ϕ_1 cloud, with most of its energy

⁵ The ϕ_1 -axis is preferred because of our choice of the background Φ as having a vanishing ϕ_2 component. More generally, the axis of symmetry will be defined by the direction of Φ in the field space.

⁶ We would like to thank an anonymous referee for raising this interesting question.

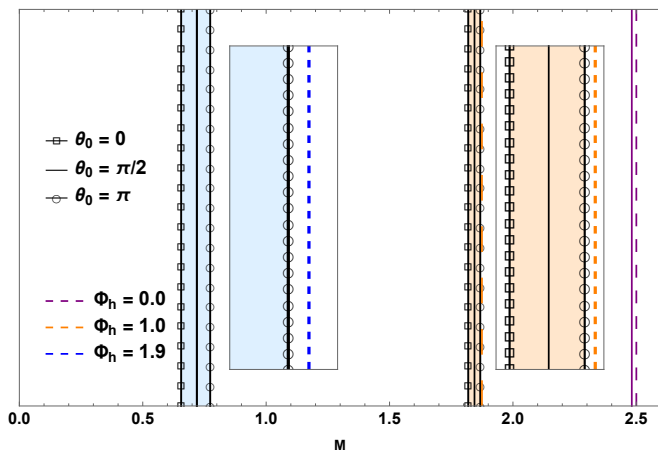


FIG. 5. *Upper panel:* Energy of initial (dashed lines) and final (solid) states. Energy loss in the $U(1)$ -symmetric phase is illustrated by the purple lines, and we consider two $U(1)$ -breaking models (orange and blue). In the latter cases, the colored bands represent the range of final values of the energy. The bands are bounded by the cases with $\theta_0 = 0$ (squares) and $\theta_0 = \pi$ (circles). The zoomed-in insets allow one to discern the energy gap between initial and final states. *Lower:* The table provides explicit data for both the initial and end states in our numerics, in particular the energy loss. Here, M_0 represents the energy of the initial state, M_1 is the energy of the end state, and ΔM_1 denotes the width of the energy band for the final states.

radiating to spatial infinity. It raises a backreaction on the field itself, which pushes the node of Φ outward from the potential well towards spatial infinity, as mentioned previously. As a result, the end state for $\theta_0 = 0$ has the minimal energy. Conversely, for the $\theta_0 = \pi$ perturbation, most of the negative ϕ_1 cloud propagates toward the black hole, driving the node of Φ into the hole to reach equilibrium. In this scenario, a minimal amount of energy from the cloud radiates to infinity, leading to the end state having maximal energy. For detailed numerical data, refer to the table in Fig. 5.

V. CONCLUSIONS

In the EMS model, the non-minimal coupling between the complex scalar and electromagnetic fields can induce a negative potential well near a RN black hole ($U(1)$ -symmetric phase), triggering the onset of scalarization and leading to the accretion of a scalar cloud onto the event horizon. During dynamical evolution, the accretion of scalar clouds preserves the global $U(1)$ symmetry, re-

sulting in $U(1)$ -symmetric final states with energy that is degenerate with respect to the initial perturbation phase θ_0 . Remarkably, even in the $U(1)$ -breaking phase, a negative potential well may exist in the presence of a non-trivial scalar field. Perturbations with different initial phases can induce the formation of scalar clouds within this well, which subsequently accrete through the event horizon, bringing energy to the black hole and radiating some energy to spatial infinity. Unlike the symmetry-preserving case, symmetry breaking allows for multiple accretion channels for scalar clouds with different initial phases. This phenomenon leads to varying amounts of energy radiated to spatial infinity, resulting in a lifting of degeneracy and the appearance of a band of possible final states. Moreover, symmetry breaking establishes a dominant accretion channel, acting as an attractor which draws in the majority of field trajectories.

This paper highlights the significant impact of spontaneous symmetry breaking on the dynamics of scalar cloud accretion. Our studies reveal distinctive signatures of symmetry breaking in black holes, providing compelling motivation for their exploration in astrophysical observations. The assumption of spherical symmetry in our setup is admittedly simplistic, and implies that neither electromagnetic nor gravitational radiation will be emitted during the evolution. It would be therefore interesting to relax this assumption in order to investigate these radiation channels and how the properties of the system may be assessed through their observation. Future research could also extend these findings to more realistic systems, such as rotating black holes, where the super-radiance phenomenon is likely to produce richer scalar cloud structures and dynamics.

Acknowledgements. We are grateful to Yupeng Zhang and Shenkai Qiao for useful discussions and valuable comments. SGS, GG and XW are supported by the NSFC (Grant Nos. 12250410250 and 12347133). PW is supported in part by the NSFC (Grant Nos. 12105191, 12275183, 12275184 and 11875196).

Appendix A: Numerical scheme for black hole evolution

In this paper, we simulate the black hole evolution using the $3+1$ decomposition of the metric, expressed as

$$ds^2 = -N_0^2 dt^2 + \gamma_{ij} (dx^i + N^i dt) (dx^j + N^j dt). \quad (\text{A1})$$

For the gravity sector, we apply the BSSN formulation, using the $1+\log$ slicing and Gamma-driver shift conditions [47–52].

To model the scalar field, we employ dynamical variables Φ and Π , where $\Pi = n^\mu \nabla_\mu \Phi$, where n_μ is given by $n_\mu = (-N_0, 0, 0, 0)$, as the 4-vector orthogonal to the spatial hypersurface. For the electromagnetic field, we decompose $F_{\mu\nu}$ into the 3-dimensional electric and magnetic components, defined as $E_i = \gamma_i^\mu n^\nu F_{\mu\nu}$ and

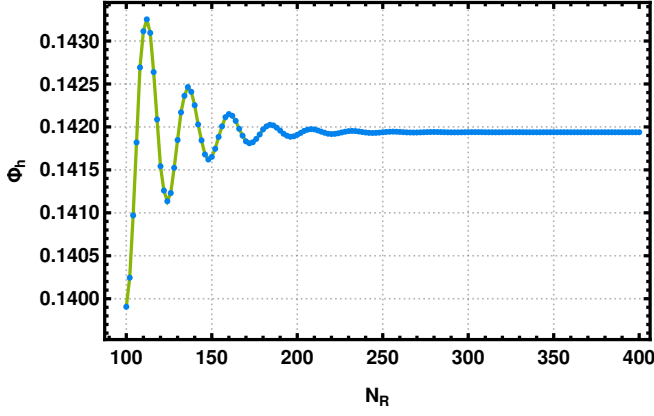


FIG. 6. Convergence test of the numerical scheme, illustrated by the event-horizon value $|\Phi_h|$ of the scalar field as function of the number N_R of grid points. The blue dots represent the final state of spontaneous scalarization from a RN black hole with $Q/M = 0.5$ and $\alpha = 160$. As the grid number increases, $|\Phi_h|$ converges, indicating convergence of the simulation.

$B_i = \gamma_i^\mu n^\nu * F_{\mu\nu}$, respectively, where $*$ denotes the Hodge dual, and γ_i^μ projects 4-dimensional vectors onto the spatial hypersurface. Since we focus on spherically symmetric evolution, the magnetic field B_i vanishes during the simulation. The evolution equations for the matter fields read

$$\begin{aligned} \partial_\perp \Phi &= N_0 \Pi, \\ \partial_\perp \Pi &= D_i (N_0 \chi^i) + N_0 \Pi K - \frac{1}{2} \alpha N_0 \Phi e^{\alpha|\Phi|^2} F^2, \\ \partial_\perp E^i &= \alpha K E^i - 2\alpha N_0 E^i (\phi_1 \Pi_1 + \phi_2 \Pi_2), \end{aligned} \quad (\text{A2})$$

where the time derivative is defined by $\partial_\perp \equiv \partial_t - \mathcal{L}_N$, and \mathcal{L}_N is the Lie derivative along N_i ; K is the trace of the extrinsic curvature, $F^2 = -2E^i E_i$, and $\phi_{1,2}$ and $\Pi_{1,2}$ denote respectively the real and imaginary parts of ϕ and Π .

During the evolution, the gravity-matter interaction is described by the stress-energy tensor $T_{\mu\nu}$, given by

$$\begin{aligned} T_{\mu\nu} &= \frac{1}{8\pi} \left(2\partial_{(\mu} \Phi^* \partial_{\nu)} \Phi - g_{\mu\nu} |\partial\Phi|^2 \right) \\ &+ \frac{1}{8\pi} e^{\alpha|\Phi|^2} \left(2F_{\mu\rho} F_{\nu}{}^\rho - \frac{1}{2} g_{\mu\nu} F^2 \right). \end{aligned} \quad (\text{A3})$$

To incorporate the matter contribution into the BSSN formalism, we project the stress-energy tensor onto 3+1

variables,

$$\begin{aligned} \rho &= n^\mu n^\nu T_{\mu\nu} = \frac{1}{8\pi} \gamma^{ij} (\partial_i \phi_1 \partial_j \phi_1 + \partial_i \phi_2 \partial_j \phi_2) \\ &+ \frac{1}{8\pi} \left(\Pi_1 \Pi_1 + \Pi_2 \Pi_2 e^{\alpha|\Phi|^2} E^2 \right), \\ J_i &= -\gamma_i^\mu n^\nu T_{\mu\nu} = -\frac{1}{4\pi} (\partial_i \phi_1 \Pi_1 + \partial_i \phi_2 \Pi_2), \\ S_{ij} &= \gamma_i^\mu \gamma_j^\nu T_{\mu\nu} \\ &= \frac{1}{4\pi} \left(\partial_i \phi_1 \partial_j \phi_1 + \partial_i \phi_2 \partial_j \phi_2 - e^{\alpha|\Phi|^2} E_i E_j \right) \\ &- \frac{1}{8\pi} \gamma_{ij} \gamma^{kl} (\partial_k \phi_1 \partial_l \phi_1 + \partial_k \phi_2 \partial_l \phi_2) \\ &+ \frac{1}{8\pi} \gamma_{ij} \left(\Pi_1 \Pi_1 + \Pi_2 \Pi_2 + e^{\alpha|\Phi|^2} E^2 \right). \end{aligned} \quad (\text{A4})$$

In our numerical simulations, we adopt a spherical-like coordinate system, introducing a dimensionless radial coordinate R to replace the standard spherical radial coordinate r . The relationship between r and R is defined as

$$r = r_{\max} \left(R_0 + \frac{e^{R/a} - e^{-R/a}}{e^{1/a} - e^{-1/a}} \right), \quad (\text{A5})$$

where r_{\max} denotes the outer boundary, and R_0 and a are scaling constants that map between r and R . Since we focus on a spherically symmetric spacetime, the radial direction R is discretized uniformly with N_R grid points, while $N_\theta = N_\varphi = 1$ for the angular directions (θ, φ) .

In Fig. 6, we present a convergence test for the simulation of spontaneous scalarization of a RN black hole, evaluated across different grid resolutions N_R . In the simulation setup, the radial coordinate parameters are specified as $r_{\max} = 30000$, $r_0 = 0.00012$ and $a = 0.07$ (recall that we use units such that $Q = 1$). The integration time step Δt is chosen to match the smallest spatial Δr_{\min} (i.e., $\Delta t = \Delta r_{\min}$) to avoid numerical instabilities. Our numerical results indicate that the simulation converges with increasing grid number N_R .

Appendix B: Radial-angular scalar field decomposition

In this Appendix we expand on the relationship between the dominant path observed in the scalar cloud accretion channels and the question of energy distribution among the field components. At a qualitative level, and at first approximation, the attractor trajectory in Fig. 4 (black curves in bottom left panel) appears to correspond to circular motion, suggesting that the energy density of the scalar field is predominantly in the angular field. This agrees with the expectation that most of the energy should go to the gapless degrees of freedom in the system, with a comparatively smaller amount going to the radial part of the scalar field.

We can confirm this intuition through an explicit calculation of the energy density of each field component,

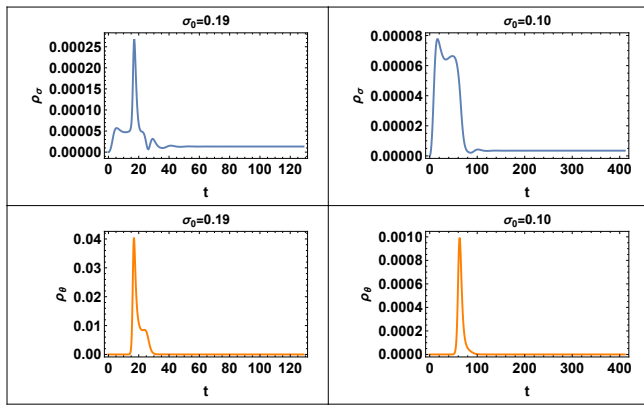


FIG. 7. Time evolution of the energy densities ρ_σ and ρ_θ , evaluated at the event horizon, and using the initial values $\sigma_0 = 0.19$ and $\sigma_0 = 0.10$. One observes that both the radial and angular fields experience a peak in the energy density corresponding to the process of accretion onto the black hole.

with the radial and angular fields defined via

$$\Phi = \sigma(x)e^{i\theta(x)}. \quad (\text{B1})$$

We define the stress-energy tensors associated to σ and

θ by

$$\begin{aligned} T_{\mu\nu}^{(\sigma)} &\equiv T_{\mu\nu} \Big|_{\theta=\theta_0, A=0} \\ &= \frac{1}{8\pi} (2\partial_\mu\sigma\partial_\nu\sigma - g_{\mu\nu}\partial^\rho\sigma\partial_\rho\sigma), \\ T_{\mu\nu}^{(\theta)} &\equiv T_{\mu\nu} \Big|_{\sigma=\sigma_0, A=0} \\ &= \frac{1}{8\pi} (2\sigma_0^2\theta^2\partial_\mu\theta\partial_\nu\theta - g_{\mu\nu}\theta^2\sigma_0^2\partial^\rho\theta\partial_\rho\theta), \end{aligned} \quad (\text{B2})$$

and the energy density of each component is given by $\rho_a = n^\mu n^\nu T_{\mu\nu}^{(a)}$ (cf. (A4)).

The time dependence of ρ_σ and ρ_θ is shown in Fig. 7 for the same simulations considered in the main text (cf. in particular Fig. 5). The results make it clear that the peak energy density of the angular field dominates over the peak value for the radial field, at least by an order of magnitude. Also noteworthy is the fact that the peak in ρ_θ has a relatively short duration, compared to the typical timescale for the accretion process. This is further illustrated in Fig. 8, which shows that most of the field trajectory is traversed in the comparatively short time interval during which the angular field dominates the energy budget.

-
- [1] B.P. Abbott et al. Observation of Gravitational Waves from a Binary Black Hole Merger. *Phys. Rev. Lett.*, 116(6):061102, 2016.
- [2] Piotr T. Chrusciel, Joao Lopes Costa, and Markus Heusler. Stationary Black Holes: Uniqueness and Beyond. *Living Rev. Rel.*, 15:7, 2012.
- [3] Richard H. Price and Gaurav Khanna. Gravitational wave sources: reflections and echoes. *Class. Quant. Grav.*, 34(22):225005, 2017.
- [4] Matthew Giesler, Maximiliano Isi, Mark A. Scheel, and Saul Teukolsky. Black Hole Ringdown: The Importance of Overtones. *Phys. Rev. X*, 9(4):041060, 2019.
- [5] Kazunori Akiyama et al. First M87 Event Horizon Telescope Results. I. The Shadow of the Supermassive Black Hole. *Astrophys. J. Lett.*, 875:L1, 2019.
- [6] Kazunori Akiyama et al. First Sagittarius A* Event Horizon Telescope Results. I. The Shadow of the Supermassive Black Hole in the Center of the Milky Way. *Astrophys. J. Lett.*, 930(2):L12, 2022.
- [7] Feng Yuan and Ramesh Narayan. Hot Accretion Flows Around Black Holes. *Ann. Rev. Astron. Astrophys.*, 52:529–588, 2014.
- [8] J. García et al. Improved Reflection Models of Black-Hole Accretion Disks: Treating the Angular Distribution of X-rays. *Astrophys. J.*, 782(2):76, 2014.
- [9] Jonathan C. McKinney, Alexander Tchekhovskoy, and Roger D. Blandford. General Relativistic Magnetohydrodynamic Simulations of Magnetically Choked Accretion Flows around Black Holes. *Mon. Not. Roy. Astron. Soc.*, 423:3083, 2012.
- [10] Kazunori Akiyama et al. First M87 Event Horizon Telescope Results. VIII. Magnetic Field Structure near The Event Horizon. *Astrophys. J. Lett.*, 910(1):L13, 2021.
- [11] Omer Blaes. General Overview of Black Hole Accretion Theory. *Space Sci. Rev.*, 183(1-4):21–41, 2014.
- [12] B. P. Abbott et al. Tests of general relativity with GW150914. *Phys. Rev. Lett.*, 116(22):221101, 2016. [Erratum: *Phys.Rev.Lett.* 121, 129902 (2018)].
- [13] B. . P. . Abbott et al. GW170608: Observation of a 19-solar-mass Binary Black Hole Coalescence. *Astrophys. J. Lett.*, 851:L35, 2017.
- [14] Benjamin P. Abbott et al. GW170104: Observation of a 50-Solar-Mass Binary Black Hole Coalescence at Redshift 0.2. *Phys. Rev. Lett.*, 118(22):221101, 2017. [Erratum: *Phys.Rev.Lett.* 121, 129901 (2018)].
- [15] R. Abbott et al. Tests of General Relativity with GWTC-3. 12 2021.
- [16] Jacob D. Bekenstein. Nonexistence of baryon number for static black holes. *Phys. Rev. D*, 5:1239–1246, 1972.
- [17] J. D. Bekenstein. Novel “no-scalar-hair” theorem for black holes. *Phys. Rev. D*, 51(12):R6608, 1995.
- [18] Carlos A.R. Herdeiro and Eugen Radu. Asymptotically flat black holes with scalar hair: a review. *Int. J. Mod. Phys. D*, 24(09):1542014, 2015.
- [19] Thomas P. Sotiriou and Shuang-Yong Zhou. Black hole hair in generalized scalar-tensor gravity. *Phys. Rev. Lett.*, 112:251102, 2014.
- [20] G. Antoniou, A. Bakopoulos, and P. Kanti. Evasion of No-Hair Theorems and Novel Black-Hole Solutions in Gauss-Bonnet Theories. *Phys. Rev. Lett.*, 120(13):131102, 2018.
- [21] Jun Zhang and Huan Yang. Dynamic Signatures of Black Hole Binaries with Superradiant Clouds. *Phys. Rev. D*, 101(4):043020, 2020.

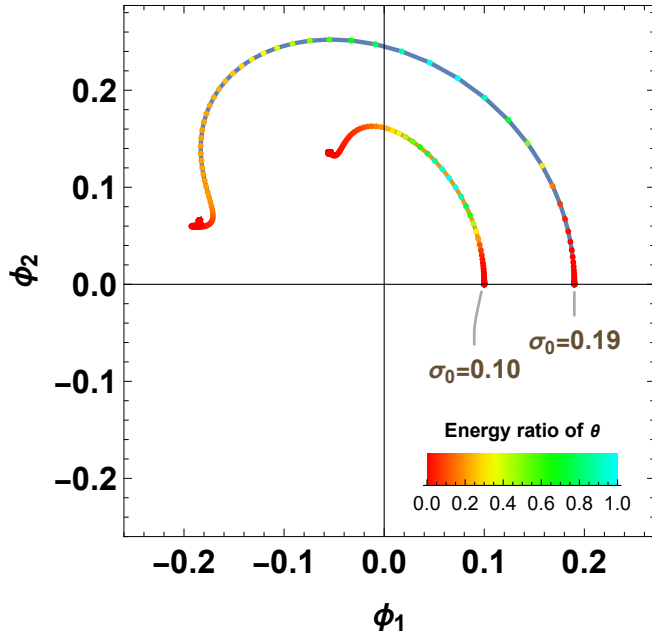


FIG. 8. Trajectory of the horizon value of the scalar field, Φ_h , in the $\phi_1 - \phi_2$ plane, using the initial values $\sigma_0 = 0.19$ and $\sigma_0 = 0.10$. Dots are separated by equal time intervals, and their color indicates the ratio of ρ_θ to its maximum value.

- [22] Daniel Baumann, Horng Sheng Chia, John Stout, and Lotte ter Haar. The Spectra of Gravitational Atoms. *JCAP*, 12:006, 2019.
- [23] Daniel Baumann, Gianfranco Bertone, John Stout, and Giovanni Maria Tomaselli. Sharp Signals of Boson Clouds in Black Hole Binary Inspirals. *Phys. Rev. Lett.*, 128(22):221102, 2022.
- [24] Marco O. P. Sampaio, Carlos Herdeiro, and Mengjie Wang. Marginal scalar and Proca clouds around Reissner-Nordström black holes. *Phys. Rev. D*, 90(6):064004, 2014.
- [25] Thibault Damour and Gilles Esposito-Farese. Nonperturbative strong field effects in tensor - scalar theories of gravitation. *Phys. Rev. Lett.*, 70:2220–2223, 1993.
- [26] Daniela D. Doneva and Stoytcho S. Yazadjiev. New Gauss-Bonnet Black Holes with Curvature-Induced Scalarization in Extended Scalar-Tensor Theories. *Phys. Rev. Lett.*, 120(13):131103, 2018.
- [27] Hector O. Silva, Jeremy Sakstein, Leonardo Gualtieri, Thomas P. Sotiriou, and Emanuele Berti. Spontaneous scalarization of black holes and compact stars from a Gauss-Bonnet coupling. *Phys. Rev. Lett.*, 120(13):131104, 2018.
- [28] Pedro V.P. Cunha, Carlos A.R. Herdeiro, and Eugen Radu. Spontaneously Scalarized Kerr Black Holes in Extended Scalar-Tensor-Gauss-Bonnet Gravity. *Phys. Rev. Lett.*, 123(1):011101, 2019.
- [29] Carlos A. R. Herdeiro, Eugen Radu, Hector O. Silva, Thomas P. Sotiriou, and Nicolás Yunes. Spin-induced scalarized black holes. *Phys. Rev. Lett.*, 126(1):011103, 2021.
- [30] Emanuele Berti, Lucas G. Collodel, Burkhard Kleihaus, and Jutta Kunz. Spin-induced black-hole scalarization in Einstein-scalar-Gauss-Bonnet theory. *Phys. Rev. Lett.*, 126(1):011104, 2021.
- [31] Carlos A.R. Herdeiro, Eugen Radu, Nicolas Sanchis-Gual, and José A. Font. Spontaneous Scalarization of Charged Black Holes. *Phys. Rev. Lett.*, 121(10):101102, 2018.
- [32] Ivan Zh. Stefanov, Stoytcho S. Yazadjiev, and Michail D. Todorov. Phases of 4D scalar-tensor black holes coupled to Born-Infeld nonlinear electrodynamics. *Mod. Phys. Lett. A*, 23:2915–2931, 2008.
- [33] Pedro G. S. Fernandes, Carlos A. R. Herdeiro, Alexandre M. Pombo, Eugen Radu, and Nicolas Sanchis-Gual. Spontaneous Scalarisation of Charged Black Holes: Coupling Dependence and Dynamical Features. *Class. Quant. Grav.*, 36(13):134002, 2019. [Erratum: *Class.Quant.Grav.* 37, 049501 (2020)].
- [34] Jose Luis Blázquez-Salcedo, Carlos A.R. Herdeiro, Jutta Kunz, Alexandre M. Pombo, and Eugen Radu. Einstein-Maxwell-scalar black holes: the hot, the cold and the bald. *Phys. Lett. B*, 806:135493, 2020.
- [35] Pedro G.S. Fernandes, Carlos A.R. Herdeiro, Alexandre M. Pombo, Eugen Radu, and Nicolas Sanchis-Gual. Charged black holes with axionic-type couplings: Classes of solutions and dynamical scalarization. *Phys. Rev. D*, 100(8):084045, 2019.
- [36] Yun Soo Myung and De-Cheng Zou. Instability of Reissner-Nordström black hole in Einstein-Maxwell-scalar theory. *Eur. Phys. J. C*, 79(3):273, 2019.
- [37] Qingyu Gan, Peng Wang, Houwen Wu, and Haitang Yang. Photon spheres and spherical accretion image of a hairy black hole. *Phys. Rev. D*, 104(2):024003, 2021.
- [38] Qingyu Gan, Peng Wang, Houwen Wu, and Haitang Yang. Photon ring and observational appearance of a hairy black hole. *Phys. Rev. D*, 104(4):044049, 2021.
- [39] Guangzhou Guo, Peng Wang, Houwen Wu, and Haitang Yang. Quasinormal modes of black holes with multiple photon spheres. *JHEP*, 06:060, 2022.
- [40] Guangzhou Guo, Yuhang Lu, Peng Wang, Houwen Wu, and Haitang Yang. Black holes with multiple photon spheres. *Phys. Rev. D*, 107(12):124037, 2023.
- [41] Guangzhou Guo, Peng Wang, Houwen Wu, and Haitang Yang. Superradiance instabilities of charged black holes in Einstein-Maxwell-scalar theory. *JHEP*, 07:070, 2023.
- [42] Guangzhou Guo, Peng Wang, Tianshu Wu, and Haitang Yang. Stationary Scalar Clouds around Kerr-Newman Black Holes. 8 2024.
- [43] Boris Latosh and Miok Park. Hairy black holes by spontaneous symmetry breaking. *Phys. Rev. D*, 110(2):024012, 2024.
- [44] Young-Hwan Hyun, Boris Latosh, and Miok Park. Scalar field perturbation of hairy black holes in EsGB theory. *JHEP*, 08:163, 2024.
- [45] Guangzhou Guo, Peng Wang, and Yupeng Zhang. Non-linear Stability of Black Holes with a Stable Light Ring. 3 2024.
- [46] Ian Ruchlin et al. Zachariah B. Etienne. Black-Holes@Home, 2022, To find out more, visit <https://blackholesathome.net/>.
- [47] C. Bona, T. Ledvinka, C. Palenzuela, and M. Zacek. General covariant evolution formalism for numerical relativity. *Phys. Rev. D*, 67:104005, 2003.
- [48] J. David Brown. Covariant formulations of BSSN and the standard gauge. *Phys. Rev. D*, 79:104029, 2009.
- [49] Zachariah B. Etienne, John G. Baker, Vasileios Pascha-

- lidis, Bernard J. Kelly, and Stuart L. Shapiro. Improved Moving Puncture Gauge Conditions for Compact Binary Evolutions. *Phys. Rev. D*, 90(6):064032, 2014.
- [50] Ian Ruchlin, Zachariah B. Etienne, and Thomas W. Baumgarte. SENR/NRPy+: Numerical Relativity in Singular Curvilinear Coordinate Systems. *Phys. Rev. D*, 97(6):064036, 2018.
- [51] Zachariah B. Etienne. Improved Moving-Puncture Techniques for Compact Binary Simulations. 4 2024.
- [52] Thomas W. Baumgarte, Pedro J. Montero, Isabel Cordero-Carrion, and Ewald Muller. Numerical Relativity in Spherical Polar Coordinates: Evolution Calculations with the BSSN Formulation. *Phys. Rev. D*, 87(4):044026, 2013.
- [53] Zachariah Etienne, Steven R. Brandt, and Peter Diener et al. The Einstein Toolkit, 2021, To find out more, visit <http://einsteintoolkit.org>.
- [54] Charles W. Misner, K. S. Thorne, and J. A. Wheeler. *Gravitation*. W. H. Freeman, San Francisco, 1973.